J/ψ production at low transverse momentum in p+p and d + Au collisions at sqrt[s_{NN}]=200 GeV

L. Adamczyk *et al.* (STAR Collaboration)

J/ψ production at low transverse momentum in $p+p$ and $d+$Au collisions at $\sqrt{s_{NN}} = 200$ GeV

L. Adamczyk,[1] J. K. Adkins,[20] G. Agakishiev,[18] M. M. Aggarwal,[32] Z. Ahammed,[50] I. Alekseev,[16] A. Aparin,[18] D. Arkhipkin,[3] E. C. Aschenauer,[3] A. Attri,[32] G. S. Averichev,[18] X. Bai,[7] V. Bairathi,[28] R. Bellwied,[46] A. Bhasin,[17] A. K. Bhati,[32] P. Bhattarai,[45] J. Bielcik,[10] J. Bielcikova,[11] L. C. Bland,[3] I. G. Bordyuzhin,[16] J. Bouchet,[19] J. D. Brandenburg,[38] A. V. Brandin,[27] I. Bunzarov,[18] J. Butterworth,[38] H. Caines,[54] M. Calderón de la Barca Sánchez,[5] J. M. Campbell,[30] D. Cebra,[5] I. Chakaberia,[3] P. Chaloupka,[10] Z. Chang,[44] A. Chatterjee,[50] S. Chattopadhyay,[50] J. H. Chen,[41] X. Chen,[22] J. Cheng,[47] M. Cherney,[9] W. Christie,[3] G. Contin,[23] H. J. Crawford,[4] S. Das,[13] L. C. De Silva,[9] R. R. Debbe,[3] T. G. Dedovich,[18] J. Deng,[40] A. A. Derevschikov,[34] B. di Ruzza,[3] L. Didenko,[3] C. Dilks,[33] X. Dong,[23] J. L. Drachenberg,[49] J. E. Draper,[5] C. M. Du,[22] L. E. Dunkelberger,[6] J. C. Dunlop,[3] L. G. Efimov,[18] J. Engelage,[4] G. Eppley,[38] R. Esha,[6] O. Evdokimov,[8] O. Eyser,[3] R. Fatemi,[20] S. Fazio,[3] P. Federic,[11] J. Fedorisin,[18] Z. Feng,[7] P. Filip,[18] Y. Fisyak,[3] C. E. Flores,[5] L. Fulek,[1] C. A. Gagliardi,[44] D. Garand,[35] F. Geurts,[38] A. Gibson,[49] M. Girard,[51] L. Greiner,[23] D. Grosnick,[49] D. S. Gunarathne,[43] Y. Guo,[39] S. Gupta,[17] A. Gupta,[17] W. Guryn,[3] A. I. Hamad,[19] A. Hamed,[44] R. Haque,[28] J. W. Harris,[54] L. He,[35] S. Heppelmann,[5] S. Heppelmann,[33] A. Hirsch,[35] G. W. Hoffmann,[45] S. Horvat,[54] T. Huang,[29] X. Huang,[47] B. Huang,[8] H. Z. Huang,[6] P. Huck,[7] T. J. Humanic,[30] G. Igo,[6] W. W. Jacobs,[15] H. Jang,[21] A. Jentsch,[45] J. Jia,[3] K. Jiang,[39] E. G. Judd,[4] S. Kabana,[19] D. Kalinkin,[15] K. Kang,[47] K. Kauder,[52] H. W. Ke,[3] D. Keane,[19] A. Kechechyan,[18] Z. H. Khan,[8] D. P. Kikoła,[51] I. Kisel,[12] A. Kisiel,[51] L. Kochenda,[27] D. D. Koetke,[49] L. K. Kosarzewski,[51] A. F. Kraishan,[43] P. Kravtsov,[27] K. Krueger,[2] L. Kumar,[32] M. A. C. Lamont,[3] J. M. Landgraf,[3] K. D. Landry,[6] J. Lauret,[3] A. Lebedev,[3] R. Lednicky,[18] J. H. Lee,[3] X. Li,[43] C. Li,[39] X. Li,[39] Y. Li,[47] W. Li,[41] T. Lin,[15] M. A. Lisa,[30] F. Liu,[7] T. Ljubicic,[3] W. J. Llope,[52] M. Lomnitz,[19] R. S. Longacre,[3] X. Luo,[7] R. Ma,[3] G. L. Ma,[41] Y. G. Ma,[41] L. Ma,[41] N. Magdy,[42] R. Majka,[54] A. Manion,[23] S. Margetis,[19] C. Markert,[45] H. S. Matis,[23] D. McDonald,[46] S. McKinzie,[23] K. Meehan,[5] J. C. Mei,[40] N. G. Minaev,[34] S. Mioduszewski,[44] D. Mishra,[28] B. Mohanty,[28] M. M. Mondal,[44] D. A. Morozov,[34] M. K. Mustafa,[23] B. K. Nandi,[14] Md. Nasim,[6] T. K. Nayak,[50] G. Nigmatkulov,[27] T. Niida,[52] L. V. Nogach,[34] S. Y. Noh,[21] J. Novak,[26] S. B. Nurushev,[34] G. Odyniec,[23] A. Ogawa,[3] K. Oh,[36] V. A. Okorokov,[27] D. Olvitt Jr.,[43] B. S. Page,[3] R. Pak,[3] Y. X. Pan,[6] Y. Pandit,[8] Y. Panebratsev,[18] B. Pawlik,[31] H. Pei,[7] C. Perkins,[4] P. Pile,[3] J. Pluta,[51] K. Poniatowska,[51] J. Porter,[23] M. Posik,[43] A. M. Poskanzer,[23] C. B. Powell,[23] N. K. Pruthi,[32] J. Putschke,[52] H. Qiu,[23] A. Quintero,[19] S. Ramachandran,[20] S. Raniwala,[37] R. Raniwala,[37] R. L. Ray,[45] H. G. Ritter,[23] R. Reed,[24] J. B. Roberts,[38] O. V. Rogachevskiy,[18] J. L. Romero,[5] L. Ruan,[3] J. Rusnak,[11] O. Rusnakova,[10] N. R. Sahoo,[44] P. K. Sahu,[13] I. Sakrejda,[23] S. Salur,[23] J. Sandweiss,[54] A. Sarkar,[14] J. Schambach,[45] R. P. Scharenberg,[35] A. M. Schmah,[23] W. B. Schmidke,[3] N. Schmitz,[25] J. Seger,[9] P. Seyboth,[25] N. Shah,[41] E. Shahaliev,[18] P. V. Shanmuganathan,[19] M. Shao,[39] A. Sharma,[17] B. Sharma,[32] M. K. Sharma,[17] W. Q. Shen,[41] Z. Shi,[23] S. S. Shi,[7] Q. Y. Shou,[41] E. P. Sichtermann,[23] R. Sikora,[1] M. Simko,[11] S. Singha,[19] M. J. Skoby,[15] N. Smirnov,[54] D. Smirnov,[3] W. Solyst,[15] L. Song,[46] P. Sorensen,[3] H. M. Spinka,[2] B. Srivastava,[35] T. D. S. Stanislaus,[49] M. Stepanov,[35] R. Stock,[12] M. Strikhanov,[27] B. Stringfellow,[35] M. Sumbera,[11] B. Summa,[33] Z. Sun,[22] X. M. Sun,[7] Y. Sun,[39] B. Surrow,[43] D. N. Svirida,[16] Z. Tang,[39] A. H. Tang,[3] T. Tarnowsky,[26] A. Tawfik,[53] J. Thäder,[23] J. H. Thomas,[23] A. R. Timmins,[46] D. Tlusty,[38] T. Todoroki,[3] M. Tokarev,[18] S. Trentalange,[6] R. E. Tribble,[44] P. Tribedy,[3] S. K. Tripathy,[13] O. D. Tsai,[6] T. Ullrich,[3] D. G. Underwood,[2] I. Upsal,[30] G. Van Buren,[3] G. van Nieuwenhuizen,[3] M. Vandenbroucke,[43] R. Varma,[14] A. N. Vasiliev,[34] R. Vertesi,[11] F. Videbæk,[3] S. Vokal,[18] S. A. Voloshin,[52] A. Vossen,[15] F. Wang,[35] G. Wang,[6] J. S. Wang,[22] H. Wang,[3] Y. Wang,[7] Y. Wang,[47] G. Webb,[3] J. C. Webb,[3] L. Wen,[6] G. D. Westfall,[26] H. Wieman,[23] S. W. Wissink,[15] R. Witt,[48] Y. Wu,[19] Z. G. Xiao,[47] W. Xie,[35] G. Xie,[39] K. Xin,[38] Y. F. Xu,[41] Q. H. Xu,[40] N. Xu,[23] H. Xu,[22] Z. Xu,[3] J. Xu,[7] S. Yang,[39] Y. Yang,[29] Y. Yang,[7] C. Yang,[39] Y. Yang,[22] Q. Yang,[39] Z. Ye,[8] Z. Ye,[8] P. Yepes,[38] L. Yi,[54] K. Yip,[3] I. -K. Yoo,[36] N. Yu,[7] H. Zbroszczyk,[51] W. Zha,[39] X. P. Zhang,[47] Y. Zhang,[39] J. Zhang,[40] J. Zhang,[22] S. Zhang,[41] S. Zhang,[39] Z. Zhang,[41] J. B. Zhang,[7] J. Zhao,[35] C. Zhong,[41] L. Zhou,[39] X. Zhu,[47] Y. Zoulkarneeva,[18] and M. Zyzak[12]

(STAR Collaboration)

[1]*AGH University of Science and Technology, FPACS, Cracow 30-059, Poland*
[2]*Argonne National Laboratory, Argonne, Illinois 60439*
[3]*Brookhaven National Laboratory, Upton, New York 11973*
[4]*University of California, Berkeley, California 94720*
[5]*University of California, Davis, California 95616*
[6]*University of California, Los Angeles, California 90095*

^{7}Central China Normal University, Wuhan, Hubei 430079
^{8}University of Illinois at Chicago, Chicago, Illinois 60607
^{9}Creighton University, Omaha, Nebraska 68178
^{10}Czech Technical University in Prague, FNSPE, Prague, 115 19, Czech Republic
^{11}Nuclear Physics Institute AS CR, 250 68 Prague, Czech Republic
^{12}Frankfurt Institute for Advanced Studies FIAS, Frankfurt 60438, Germany
^{13}Institute of Physics, Bhubaneswar 751005, India
^{14}Indian Institute of Technology, Mumbai 400076, India
^{15}Indiana University, Bloomington, Indiana 47408
^{16}Alikhanov Institute for Theoretical and Experimental Physics, Moscow 117218, Russia
^{17}University of Jammu, Jammu 180001, India
^{18}Joint Institute for Nuclear Research, Dubna, 141 980, Russia
^{19}Kent State University, Kent, Ohio 44242
^{20}University of Kentucky, Lexington, Kentucky, 40506-0055
^{21}Korea Institute of Science and Technology Information, Daejeon 305-701, Korea
^{22}Institute of Modern Physics, Chinese Academy of Sciences, Lanzhou, Gansu 730000
^{23}Lawrence Berkeley National Laboratory, Berkeley, California 94720
^{24}Lehigh University, Bethlehem, PA, 18015
^{25}Max-Planck-Institut fur Physik, Munich 80805, Germany
^{26}Michigan State University, East Lansing, Michigan 48824
^{27}National Research Nuclear Univeristy MEPhI, Moscow 115409, Russia
^{28}National Institute of Science Education and Research, Bhubaneswar 751005, India
^{29}National Cheng Kung University, Tainan 70101
^{30}Ohio State University, Columbus, Ohio 43210
^{31}Institute of Nuclear Physics PAN, Cracow 31-342, Poland
^{32}Panjab University, Chandigarh 160014, India
^{33}Pennsylvania State University, University Park, Pennsylvania 16802
^{34}Institute of High Energy Physics, Protvino 142281, Russia
^{35}Purdue University, West Lafayette, Indiana 47907
^{36}Pusan National University, Pusan 46241, Korea
^{37}University of Rajasthan, Jaipur 302004, India
^{38}Rice University, Houston, Texas 77251
^{39}University of Science and Technology of China, Hefei, Anhui 230026
^{40}Shandong University, Jinan, Shandong 250100
^{41}Shanghai Institute of Applied Physics, Chinese Academy of Sciences, Shanghai 201800
^{42}State University Of New York, Stony Brook, NY 11794
^{43}Temple University, Philadelphia, Pennsylvania 19122
^{44}Texas A&M University, College Station, Texas 77843
^{45}University of Texas, Austin, Texas 78712
^{46}University of Houston, Houston, Texas 77204
^{47}Tsinghua University, Beijing 100084
^{48}United States Naval Academy, Annapolis, Maryland, 21402
^{49}Valparaiso University, Valparaiso, Indiana 46383
^{50}Variable Energy Cyclotron Centre, Kolkata 700064, India
^{51}Warsaw University of Technology, Warsaw 00-661, Poland
^{52}Wayne State University, Detroit, Michigan 48201
^{53}World Laboratory for Cosmology and Particle Physics (WLCAPP), Cairo 11571, Egypt
^{54}Yale University, New Haven, Connecticut 06520

We report on the measurement of J/ψ production in the dielectron channel at mid-rapidity ($|y| <$ 1) in $p+p$ and $d+$Au collisions at $\sqrt{s_{NN}} = 200$ GeV from the STAR experiment at the Relativistic Heavy Ion Collider. The transverse momentum p_T spectra in $p+p$ for $p_T < 4$ GeV/c and $d+$Au collisions for $p_T < 3$ GeV/c are presented. These measurements extend the STAR coverage for J/ψ production in $p+p$ collisions to low p_T. The $\langle p_T^2 \rangle$ from the measured J/ψ invariant cross section in $p+p$ and $d+$Au collisions are evaluated and compared to similar measurements at other collision energies. The nuclear modification factor for J/ψ is extracted as a function of p_T and collision centrality in $d+$Au and compared to model calculations using the modified nuclear Parton Distribution Function and a final-state J/ψ nuclear absorption cross section.

I.   INTRODUCTION

The study of J/ψ production has been extensively used to probe the medium created in relativistic heavy-ion collisions, where a transition from hadronic matter to a deconfined Quark Gluon Plasma (QGP) takes place [1–4].

A large suppression of J/ψ was proposed as a signature of the formation of QGP and was expected to arise from the color screening of the heavy quark potential in a deconfined medium [5].

Additional modifications of J/ψ production due to Cold Nuclear Matter (CNM) effects [6] are expected. CNM effects are due to the presence of ordinary nuclear matter in the collision. These include modifications to the Parton Distribution Functions (PDFs) inside a nucleus (shadowing, anti-shadowing, EMC effect) [7] and final-state nuclear absorption of J/ψ by hadronic co-movers [8]. In addition, the Cronin effect, which may be originating from multiple scattering of partons, should increase the mean p_T of J/ψ produced in A+A collisions relative to $p+p$ collisions [9, 10]. In order to isolate the CNM effects and thereby improve our understanding of modifications to J/ψ production in heavy-ion collisions, the production of J/ψ is studied in both $p+p$ and d+Au collisions at Relativistic Heavy Ion Collider (RHIC), where the formation of a QGP was not originally expected. Furthermore, J/ψ production in $p+p$ collisions can provide information on the J/ψ production mechanism in elementary collisions [11].

In this paper, the results for J/ψ production at mid-rapidity ($|y| < 1$, where y is defined as $y = 0.5 \ln(\frac{E+p_L c}{E-p_L c})$, E is the particle's energy, p_L is the particle's momentum along beam axis and c is the speed of light in a vacuum) in $p+p$ ($p_T < 4$ GeV/c) and d+Au ($p_T < 3$ GeV/c) collisions at $\sqrt{s_{NN}} = 200$ GeV from the STAR experiment are presented. The $p+p$ data were collected in 2009 and d+Au in 2008. The p_T spectrum from $p+p$ is combined with the high-p_T STAR results [11] and the resulting p_T spectrum is compared with predictions from model calculations, including the Color Glass Condensate (CGC) along with the non-relativistic Quantum Chromodynamics (QCD) based model with Color Singlet and Color Octet (CS+CO) contributions [12], the NRQCD based CS+CO model only [13] and the Color Evaporation Model (CEM) [14]. The $\langle p_T^2 \rangle$ in both $p+p$ and d+Au collisions is calculated from the measured invariant cross sections and compared to measurements at other relevant collision energies. The value of $\langle p_T^2 \rangle$ is related to the width of the p_T spectrum and is conventionally used to describe the Cronin effect [15] in model calculations. It is described in more details further in the paper.

To quantify the CNM effects, the J/ψ nuclear modification factor in d+Au (R_{dA}) has been calculated from the ratio of the invariant cross section in d+Au ($\mathrm{d}^2\sigma_{d+\mathrm{Au}}/\mathrm{d}p_T\mathrm{d}y$) and $p+p$ ($\mathrm{d}^2\sigma_{pp}/\mathrm{d}p_T\mathrm{d}y$), scaled by the average number of binary collisions $\langle N_{\mathrm{coll}} \rangle$ according to the equation:

$$R_{dA} = \frac{1}{\langle N_{\mathrm{coll}} \rangle} \frac{\mathrm{d}^2\sigma_{d+\mathrm{Au}}/\mathrm{d}p_T\mathrm{d}y}{\mathrm{d}^2\sigma_{pp}/\mathrm{d}p_T\mathrm{d}y}. \quad (1)$$

The J/ψ R_{dA} is compared to model predictions, which include cold nuclear matter effects and the modification of nuclear PDFs (nPDFs) using the EPS09 [16] and nDSg [17] parameterizations. Each of these models includes a final-state J/ψ nuclear absorption cross section (σ_{abs}) [6, 18] as an additional parameter, which can be determined by fitting the model calculations to the data.

The experimental setup and data used in this analysis are described in Section II followed by a review of the analysis methods, J/ψ signal reconstruction, and corrections in Section III. The systematic uncertainties are explained in Section IV, and the results are described in Section V. Finally, a summary is provided in Section VI.

II. EXPERIMENT AND DATA

STAR [19] is a large acceptance mid-rapidity (pseudo-rapidity $|\eta| < 1$ and full azimuthal angle) experiment at RHIC with excellent particle identification capabilities. It also includes additional detectors at forward and backward pseudo-rapidities ($|\eta| > 1$) like Forward Time Projection Chamber (FTPC) and Vertex Position Detector (VPD) and others, which are not used in this analysis. The Time Projection Chamber (TPC) is the primary detector used for particle tracking and hadron identification while the Barrel Electro-Magnetic Calorimeter (BEMC) is used for electron identification. For the $p+p$ data, the Time of Flight detector (TOF) [20] was available for particle identification. For the d+Au data the collision centrality was determined using the East Forward Time Projection Chamber (FTPC-E) [21], which covers $-4 < \eta < -2.5$.

The data used in this analysis were obtained from $p+p$ collisions recorded in 2009 and from d+Au collisions recorded in 2008 using a minimum bias (MB) trigger. The MB trigger was generated from the Vertex Position Detectors (VPDs) [22] to select collisions with a vertex position $|V_Z| < 30$ cm by requiring coincidence signals within a bunch crossing in its East (gold facing in case of d+Au collisions) and West detectors, both located 5.7 m from the center of the TPC. The collision V_Z used in the trigger was evaluated from the time difference between VPD signals. The d+Au trigger also required at least one neutron in the East Zero Degree Calorimeter (ZDC) [23], positioned 18 m away from the center of the TPC.

The offline vertex position was reconstructed using tracks in the TPC. To remove out-of-time (pile-up) events in the p+p data sample, a difference between the reconstructed and VPD vertex position $|\Delta V_Z| < 6$ cm was required [24]. This removes $\sim 15\%$ of events and leaves $\sim 2\%$ [24] of pile-up events. In d+Au, pile-up events were removed by requiring at least one track from the collision be matched to the BEMC [25], which is a fast detector (readout time ~ 10 ns) and is not affected by pile-up. The BEMC match requirement along with $|V_Z| < 30$ cm cut rejects $\sim 35\%$ of events with the possible bias estimated at $\sim 4\%$ at most. The final data samples used in this analysis consisted of 7.7×10^7 $p+p$ and 3×10^7 d+Au events satisfying the MB trigger and pile-up removal cri-

teria.

III. ANALYSIS

A. Collision Geometry

The collision centrality in d+Au reactions was determined using the Glauber model [26] relating the measured particle multiplicity to the initial geometry. The centrality selection in d+Au was obtained using the charged particle multiplicity in the FTPC-E [21] to minimize correlations between the centrality selection and the measured event in the TPC. The centrality definitions, the corresponding average number of participants ($\langle N_{\mathrm{part}}\rangle$), number of collisions ($\langle N_{\mathrm{coll}}\rangle$), and impact parameter ($\langle b \rangle$) in d+Au collisions are summarized in Table II.

A multiplicity dependent correction was performed in d+Au to account for the trigger bias towards events with high multiplicity. This was done by comparing the multiplicity distribution measured using the TPC and FTPC-E to the distributions obtained from the Glauber model to calculate a multiplicity dependent weight. The corrections were later applied using event-by-event reweighing, which increased the overall (event integrated) weight of events in the $40 - 100\%$ centrality bin in d+Au collisions by a factor ~ 1.33, while having a negligible effect on semi-central and central collisions. The event integrated weights for d+Au are listed in the table I. An overall trigger correction of 70% [24] has been used in MB p+p collisions to account for the trigger bias towards events containing a J/ψ as discussed later.

TABLE I: Event integrated weights used for trigger bias correction in d+Au in each centrality bin.

Centrality	Weight [1]
$0 - 40\%$	1
$40 - 100\%$	~ 1.33

TABLE II: The collision centrality and geometry definitions from the Glauber model in d+Au collisions [27]. The listed errors are systematic only.

Centrality	$\langle N_{\mathrm{part}}\rangle$	$\langle N_{\mathrm{coll}}\rangle$	$\langle b \rangle$ (fm)
$0 - 40\%$	13.3 ± 2.3	12.7 ± 2.3	4.1 ± 0.8
$40 - 100\%$	5.7 ± 0.7	4.8 ± 0.6	6.7 ± 0.8

B. Particle Identification

The reconstruction of J/ψ has been performed using the dielectron decay channel $J/\psi \rightarrow e^{+} + e^{-}$ with a branching ratio of $B_{ee} = 5.961 \pm 0.033\%$ [28]. Electrons and positrons were identified from the ionization energy they deposited in the TPC. The $\mathrm{d}E/\mathrm{d}x$ versus momentum for charged particles in the TPC is shown in Fig. 1a. The lines indicate the expected $\mathrm{d}E/\mathrm{d}x$ for various particles obtained from the Bichsel functions [29].
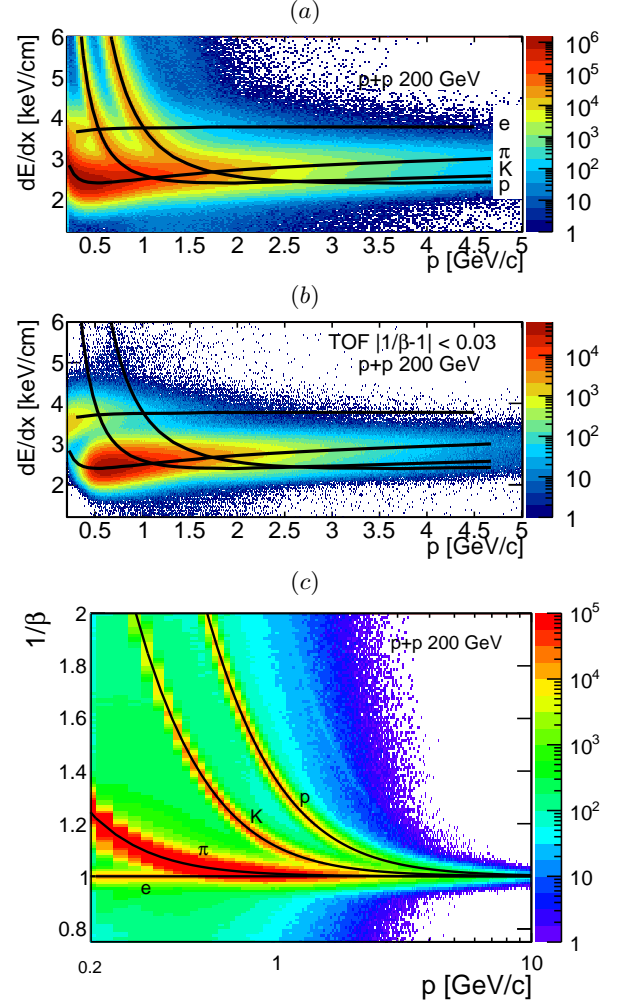

FIG. 1: (Color online) (a) The ionization energy loss $\mathrm{d}E/\mathrm{d}x$ versus momentum for charged particles in p+p collisions. The lines indicate the expected $\mathrm{d}E/\mathrm{d}x$ for various particles obtained from the Bichsel functions [29]. (b) The $\mathrm{d}E/\mathrm{d}x$ distribution after removing slower hadrons using the TOF. (c) The TOF $1/\beta$ versus momentum for charged particles in p+p collisions. The lines indicate the expected values for various particles.

The deviation of the measured $\mathrm{d}E/\mathrm{d}x$ from the ex-

pected dE/dx for an electron, $n\sigma_e$, is defined here as:

$$n\sigma_\alpha = \ln\left(\frac{dE/dx|_{Measured}}{dE/dx|_{Expected}}\right)/\sigma, \ \alpha = e, \pi, K, p. \quad (2)$$

where $dE/dx|_{Measured}$ is measured with the TPC, $dE/dx|_{Expected}$ is the expected value and σ is the resolution of the measured $\ln(dE/dx)$. To remove the large hadron contamination at low momenta where the dE/dx of electrons and hadrons overlaps, a minimum transverse momentum (p_T) of electron candidates was applied. Only tracks with $p_T > 0.8$ GeV/c in $p+p$ and $p_T > 1$ GeV/c in $d+$Au were accepted. The $n\sigma_e$ distribution for charged particles with $1.2 < p < 1.3$ GeV/c in $p+p$ and $d+$Au collisions is shown in Fig. 2 and has been fitted with the sum of Gaussian distributions to account for the individual particle contributions. The vertical lines indicate the accepted range, and the shaded region represents the electron candidates. Electrons were selected by requiring $-1 < n\sigma_e < 2$ in $p+p$ and $|n\sigma_e| < 2.4$ in $d+$Au. The asymmetric cut in $p+p$ was used to remove the large hadron contamination at $n\sigma_e < -1$. These hadrons in $d+$Au were rejected by requiring $|n\sigma_p| > 2.2$ and $|n\sigma_\pi| > 2.5$. These cuts lead to the non-regular shape of the left side of shaded area in the Fig. 2 (lower panel), where horizontal scale is in $n\sigma_e$ units. The hadron dE/dx rejection cuts were not necessary in the $p+p$ analysis, as the TOF was used to separate electrons from slow hadrons and also allowed for a lower cut on the minimum p_T in $p+p$ collisions. Because the TOF detector is only available in the $p+p$ sample, the particle identification cuts are different in $p+p$ and $d+$Au analyses. The differences are summarized in Table III.

FIG. 2: (Color online) The dE/dx $n\sigma_e$ distributions for all charged particles in $p+p$ (upper plot) and $d+$Au (lower plot) collisions with $1.2 < p < 1.3$ GeV/c. Multiple Gaussians have been fitted to the particles distribution. The vertical lines indicate the accepted range, and the shaded region shows the accepted particles. The plots are after TOF cut for $p+p$ and BEMC cuts for $d+$Au.

TABLE III: Summary of analysis cuts in $p+p$ and $d+$Au.

Cut	$p+p$	$d+$Au
p_T	> 0.8 GeV/c	> 1 GeV/c
$n\sigma_e$	$-1 < n\sigma_e < 2$	< 2.4
$|n\sigma_p|$	$-$	> 2.2
$|n\sigma_\pi|$	$-$	> 2.5
$|1/\beta - 1|$	< 0.03 for $p < 1.4$ GeV/c	$-$
E/p	> 0.5 for $p > 2$ GeV/c	> 0.5

In the $p+p$ data sample, each particle's velocity (β) is evaluated using the TOF detector. The TOF $1/\beta$ distribution in $p+p$ collisions is shown in Fig. 1c versus the momentum obtained from the track reconstruction in the TPC. The lines indicate the expected $1/\beta$ values for several particle species. The 72% of the TOF detector was installed for the $p+p$ data and it was used to improve the electron identification for $p < 1.4$ GeV/c. At higher momenta, the $1/\beta$ of electrons and hadrons converges to unity and the electron-hadron discrimination power decreases. Heavier hadrons were removed by requiring $|1/\beta - 1| < 0.03$. The resulting dE/dx distribution is shown in Fig. 1b. This cut successfully removes most
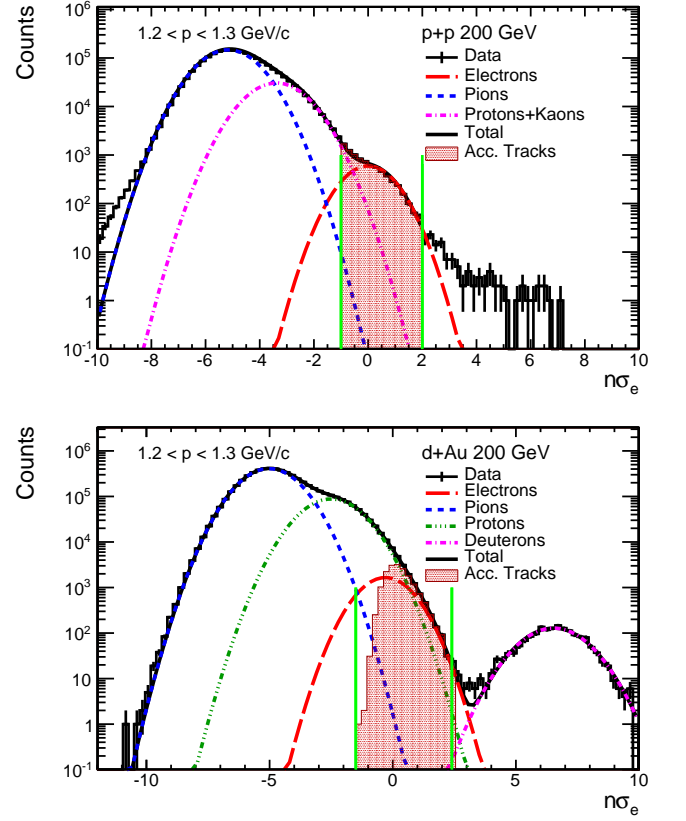
of the contributions from kaons, protons, and deuterons. The remaining pions are sufficiently well separated from the electrons and were removed using the TPC dE/dx.

Electron energy is measured using the BEMC. The BEMC has a radiation length of $20X_0$ and is segmented into towers of dimension $\Delta\eta \times \Delta\phi = 0.05 \times 0.05$. The energy deposited in its towers has been used to calculate the energy-to- momentum ratio (E/p), which should be ~ 1 for electrons. The E/p distribution is shown in Fig. 3 for electrons obtained from data and a Monte Carlo GEANT [26] simulation with STAR detector geometry. A non-Gaussian tail at low-E/p results from electrons striking near the edge of the tower and sharing their energy between multiple towers. This also causes a shift of the Gaussian to low E/p values. Electrons are identified and selected by requiring $E/p > 0.5$ for $p > 2$ GeV/c in $p+p$ and $E/p > 0.5$ in $d+$Au collisions.
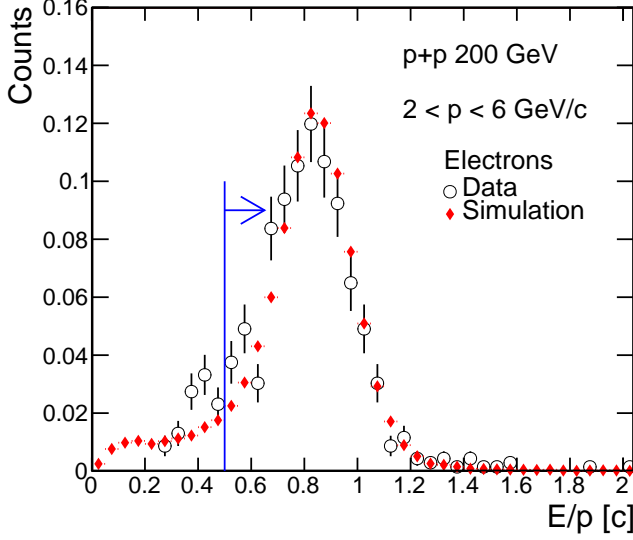
FIG. 3: (Color online) The E/p distribution for electrons with $2 < p < 6$ GeV/c in $p+p$ collisions from data (closed circles) and simulation (closed diamonds).
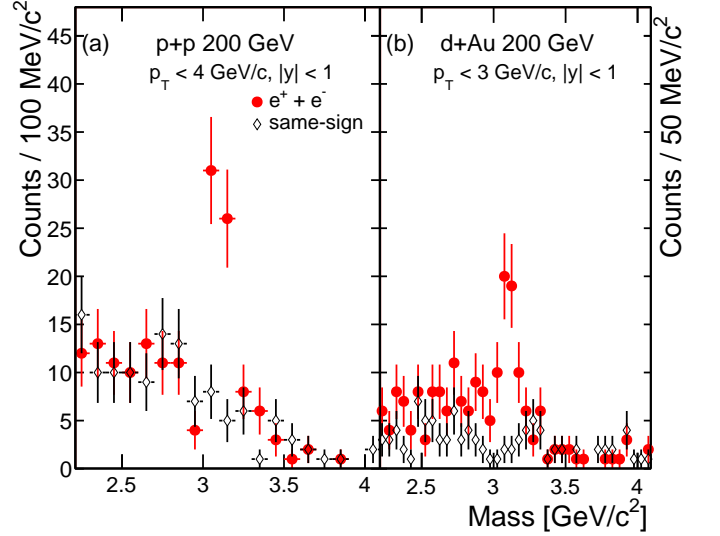

FIG. 4: (Color online) The opposite-sign dielectron invariant mass distribution in (a) $p+p$ collisions and (b) $d+$Au collisions at $\sqrt{s_{NN}} = 200$ GeV (closed circles). The combinatorial background (open diamonds) has been calculated from the same-sign pairs.
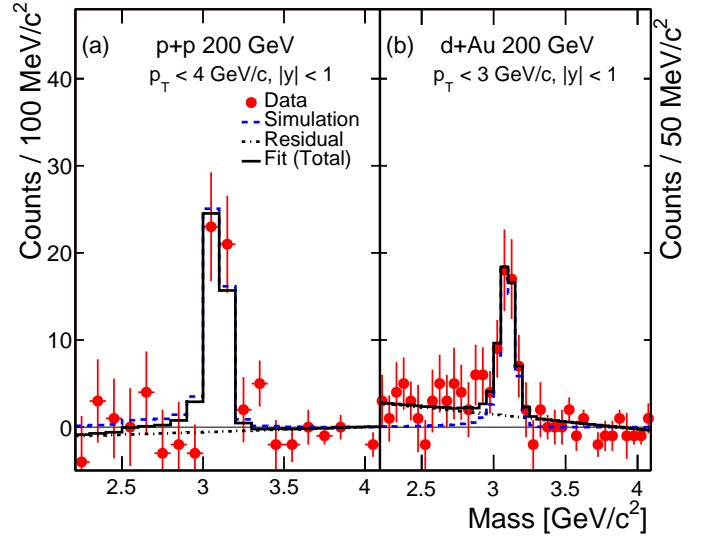
C. J/ψ Signal

The dielectron invariant mass spectrum is constructed from electrons identified using TPC, BEMC, and TOF. The resulting dielectron invariant mass spectra in $|y| < 1$ for $p_T < 4$ GeV/c in $p+p$ and $p_T < 3$ GeV/c in $d+$Au collisions at $\sqrt{s_{NN}} = 200$ GeV are shown in Fig. 4. The combinatorial background has been calculated using a sum of same-sign electron pairs ($e^+e^+ + e^-e^-$), and a signal-to-background ratio of $S/B = 0.81$ in $p+p$ and $S/B = 2.3$ in $d+$Au was obtained for $2.7 < m < 3.2$ GeV/c^2.

The J/ψ signal obtained from subtracting the combinatorial background from the dielectron invariant mass spectrum is shown in Fig. 5. The signal shape has been obtained from a Monte Carlo GEANT simulation and reflects the TPC momentum resolution and energy loss in the detector material. This shape is combined with a straight line to account for a residual background ($c\bar{c}$ continuum, Drell-Yan), and the total has been fitted to the data. The yield has been calculated by performing a bin counting of the data entries in the range $2.7 < m < 3.2$ GeV/c^2 in $p+p$ and $d+$Au collisions. The residual background has been subtracted, and the counts have been corrected for the number of J/ψ outside of this mass range using the signal shape from simulation. A total of 44 ± 14 (66 ± 10) J/ψs were obtained in $p+p$ ($d+$Au) collisions with a significance of 3.2σ (6.8σ).

FIG. 5: (Color online) The J/ψ signal for $|y| < 1$ in (a) $p+p$ collisions and (b) $d+$Au collisions at $\sqrt{s_{NN}} = 200$ GeV, after same-sign background subtraction (closed circles). The signal shape obtained from simulation (dashed line) is combined with a residual background (dot-dashed line), and the total is fitted to the data (solid line).

D. Corrections

The electron identification efficiency is defined as the ratio of accepted electrons to all electrons, while purity
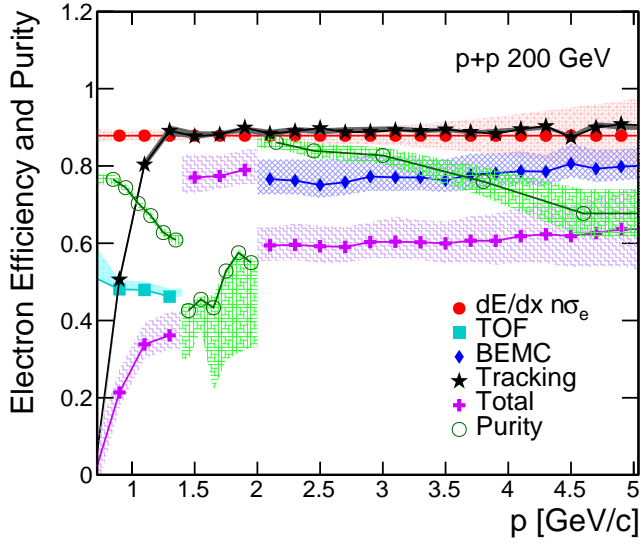
FIG. 6: (Color online) The single electron efficiencies, including the dE/dx (closed circles), TOF (closed squares), BEMC (closed diamonds), tracking (closed stars), and total (closed crosses) efficiencies and purity (open circles) in $p+p$ collisions. The shaded regions represent systematic uncertainties.

is the fraction of electrons in the selected sample. This is illustrated in Fig. 2, where the electron contribution of the $n\sigma_e$ distribution in $p+p$ collisions has been fit with a Gaussian function. The vertical lines indicate the accepted range, and the shaded region indicates the accepted particles. The efficiency is the integral of the electron Gaussian within the green lines ($-1 < n\sigma_e < 2$) divided by the integral over the entire electron Gaussian (dashed red line). The purity is calculated by taking the ratio of the integral of the electron Gaussian function within the green lines to the integral of the accepted tracks histogram (shaded area).

The efficiencies related to the electron identificiation requirements in $p+p$ are shown in Fig. 6. The $p+p$ analysis uses different detectors to identify particles at different momenta, due to their different performance, as was explained in the previous section. Electron identification is determined from the TOF and TPC at low momentum ($p < 1.4$ GeV/c), the BEMC and TPC at high momentum ($p > 2$ GeV/c), and the TPC alone for $1.4 < p < 2$ GeV/c. The abrupt changes in Fig. 6 arise from the different efficiencies of each detector. The dE/dx cut efficiency is mostly constant as no requirements were placed on the hadrons. The BEMC was used for $p > 2$ GeV/c and the combined matching and E/p efficiency are $\sim 80\%$, consistent with the BEMC efficiency in $d+$Au. The TOF has been used for $p < 1.4$ GeV/c, and the matching and $1/\beta$ efficiency are combined with the TOF accceptance to obtain a correction of $\sim 50\%$. The electron tracking efficiency is $\sim 90\%$ for $p > 1.4$ GeV/c, and decreases below this due to the

minimum p_T required for electrons. The total efficiency and purity are also shown, and a sudden drop is observed for $1.4 < p < 2$ GeV/c where only the TPC is used for particle identification in order to maximize statistics.

The efficiency associated with the dE/dx electron identification requirements in $d+$Au collisions is shown in Fig. 7. Electron identification in $d+$Au was performed using the TPC dE/dx and BEMC E/p for $p_T > 1$ GeV/c. The dE/dx identification efficiency in $d+$Au for $p < 1.4$ GeV/c is smaller than the efficiency in $p+p$ due to the hadron rejection cuts as discussed earlier. At high p_T, the efficiency decreases slightly due to the relativistic rise of the hadron dE/dx (see Fig. 1a). The purity of the electron sample obtained using the TPC dE/dx alone is depicted in Fig. 7. The purity increases by a factor ~ 2 when including the E/p cut.
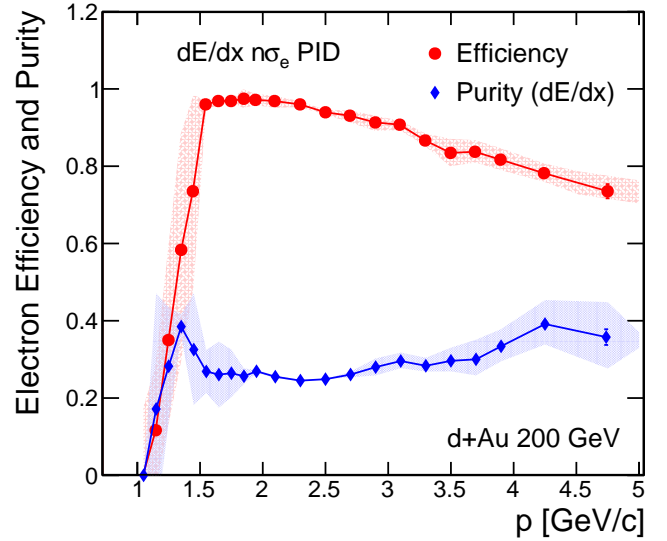

FIG. 7: (Color online) The single electron dE/dx identification efficiency (circles) and purity obtained in $d+$Au collisions. The shaded areas correspond to systematic uncertainty.

The total J/ψ tracking efficiency and acceptance in $|y| < 1$ have been obtained from a GEANT simulation, and are shown in Fig. 8 for $p+p$ and $d+$Au. A lower efficiency was observed in $d+$Au due to the higher minimum p_T required for electrons. The tracking efficiency and acceptance have been combined with the electron identification efficiencies to obtain the total J/ψ efficiency corrections also shown in Fig. 8. An additional trigger correction of 70% [24] has been applied to the $p+p$ data to account for the VPD selection bias towards events containing a J/ψ. This 70% correction was determined by comparing the number of events containing at least one J/ψ to the number of unbiased events in a Monte Carlo PYTHIA simulation coupled with the STAR detector geometry [24].
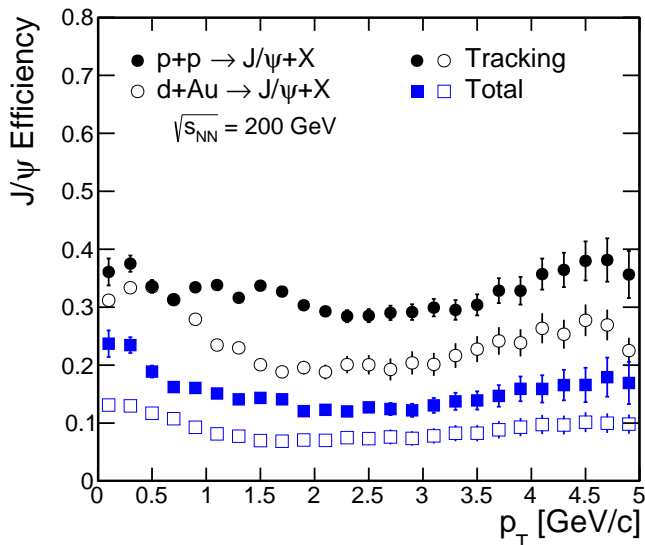
FIG. 8: (Color online) The J/ψ tracking efficiency and acceptance (circles) is combined with the electron identification efficiency to determine the total J/ψ efficiency (squares) in $p+p$ collisions (closed symbols) and $d+$Au collisions (open symbols).

IV.   SYSTEMATIC UNCERTAINTIES

The main sources of systematic uncertainties on the yield in $p+p$ and $d+$Au collisions arise from the uncertainty in the corrections and yield extraction procedure. These are investigated separately in each J/ψ p_T bin, while the uncertainties on the integrated yield are reported in the text. The multiple Gaussian fits to the $n\sigma_e$ distribution and the calculation of the efficiency from the dE/dx requirements using these fits resulted in an uncertainty of 6% in $p+p$ and a higher 16% in $d+$Au collisions due to lack of TOF. The uncertainty on the BEMC matching and E/p efficiency was found to be 9% (11%) in $p+p$ ($d+$Au) and was estimated by comparing the efficiency obtained from a high purity electron sample from the data to the efficiency obtained from simulation. An additional 4% systematic uncertainty due to the TOF requirement in $p+p$ collisions was estimated by comparing the efficiency from electrons and hadrons. The tracking efficiency was obtained from a GEANT simulation, from which comparison between the track properties from simulation and data resulted in an uncertainty of 3% in $p+p$ collisions. A higher uncertainty of 12% in $d+$Au collisions was obtained due to higher backgrounds. The shape of the input rapidity and p_T distributions in simulation were varied to determine the effect on the p_T-dependent and p_T- integrated efficiency calculation, and an uncertainty on the final yield of 8% (9%) was determined from the efficiency correction in $p+p$ ($d+$Au) collisions. The uncertainty on the yield was calculated by changing the mass window in which the counting was performed, and

TABLE IV: The systematic uncertainties on the yield in $p+p$ and $d+$Au collisions.

Source	Relative Uncertainty (%)	
	$p+p$	$d+$Au
eID (TPC)	±6	$+16\ -11$
eID (BEMC)	±9	±11
eID (TOF)	±4	$-$
Tracking	±3	±12
Efficiency Corr.	±8	±9
Yield	±44	±23
Total	±46	±33
$N_{\rm coll}$	$-$	±12
σ^{p+p}	±8	±8

comparing the yield to that obtained from the integral of the signal shape from simulation. This resulted in an uncertainty of 40% in $p+p$ collisions and 15% in $d+$Au collisions. An additional 4% uncertainty due to the contribution from internal radiation (J/$\psi \to e^+e^-\gamma$) was also included. The effect of possible bias due to pile-up events removal with the BEMC in $d+$Au, was estimated to be 4% at most.

The normalization uncertainty on the nuclear modification factor R_{dA} (Eq. 1) combines the uncertainty on $N_{\rm coll}$ of 12%, and the statistical and systematic uncertainty of the J/ψ cross section in $p+p$ for $p_T < 3$ GeV/c. The systematic uncertainty includes the normalization uncertainty for the inelastic cross section in $p+p$ (σ^{p+p}) of 8% [30]. The systematic uncertainties in $p+p$ for $p_T < 4$ GeV/c and $d+$Au collisions are summarized in Table IV.

V.   RESULTS

The J/ψ invariant cross section in $p+p$ collisions at $\sqrt{s_{NN}} = 200$ GeV and the J/ψ invariant yield in $d+$Au at $\sqrt{s_{NN}} = 200$ GeV are shown as functions of p_T in Fig. 9. The p_T spectrum in $p+p$ (left panel) extends the full STAR p_T coverage to $0 < p_T < 14$ GeV/c [11] and is consistent with previously published data from PHENIX [31] at much smaller acceptance $|y| < 0.35$. The data are compared to the Color Evaporation Model (CEM) [14] for prompt J/ψ production in $p+p$ collisions. The CEM is able to describe the data well for the entire range of transverse momentum, while it does not include contributions from B decay which is expected to be $10 - 25\%$ for $p_T > 4$ GeV/c and decreasing at lower p_T [11]. The model includes feed-down from heavier charmonium states (χ_c and ψ'), which are expected to contribute up to 40% of the produced J/ψ yield [33]. The data are also compared to the non-relativistic Quantum Chromodynamics (NRQCD) calculations at next-to-leading order (NLO) with Color Singlet and Color Octet (CS+CO) contributions [13] for prompt J/ψ production
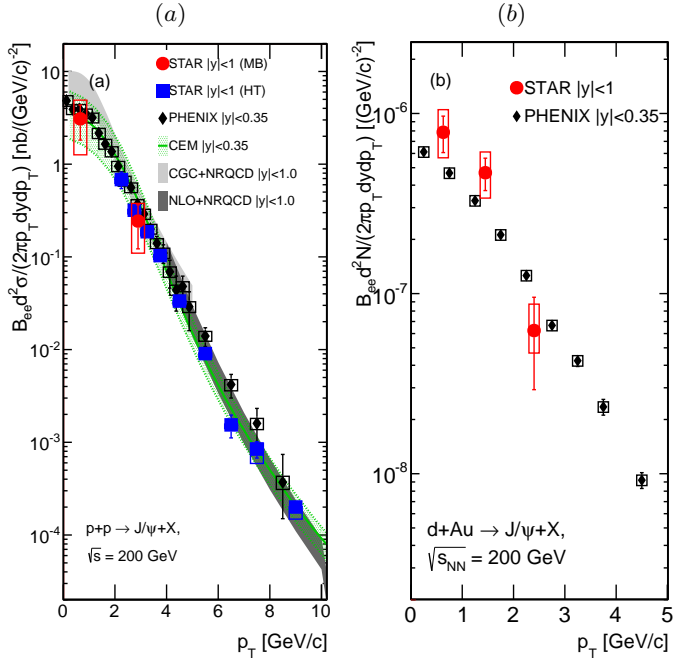
FIG. 9: (Color online) (a) The invariant cross section versus transverse momentum for J/ψ with $|y| < 1$ in p+p collisions (closed circles), compared to high-p_T STAR data [11] in $|y| < 1$ (closed squares), PHENIX data in $|y| < 0.35$ [31] (closed diamonds), and various model predictions [12–14]. (b) The invariant yield versus transverse momentum for J/ψ with $|y| < 1$ in $0 - 100\%$ central d+Au collisions (closed circles). This is compared to PHENIX data in $|y| < 0.35$ [32] (closed diamonds).

in p+p collisions for $p_T > 4$ GeV/c. The model describes the data within large uncertainties, altough it does not include contributions from B meson decays. It also includes feed-down from χ_c and ψ'. The Color Glass Condensate (CGC) NLO CS+CO NRQCD model [12] for prompt J/ψ for $p_T < 5$ GeV/c also describes the data within sizeable uncertainties.

The J/ψ p_T spectrum in d+Au measured by STAR (right panel) compared to PHENIX data taken at $|y| < 0.35$ [32], shows consistency within present statistical and systematic uncertainties. The resulting slope difference is consistent with zero within these uncertainties.

The integrated cross section for J/ψ production in p+p collisions for $|y| < 1$ at STAR has been calculated using the low-p_T STAR data for $p_T < 2$ GeV/c combined with the previously published high-p_T data for $p_T > 2$ GeV/c [11] and is found to be:

$$B_{ee}\frac{\mathrm{d}\sigma_{J/\psi}}{\mathrm{d}y} = 38 \pm 11 \ \text{(stat.)} \pm 16 \ \text{(syst.) nb.} \quad (3)$$

where the systematic uncertainty includes the uncertainty on the inelastic cross section in p+p of 8%.

PHENIX data at low p_T ($p_T < 2$ GeV/c) have smaller

statistical uncertainties compared to STAR measurements and therefore were used as a baseline for R_{dA}. The integrated cross section was also re-calculated using the PHENIX data for $p_T < 2$ GeV/c. The value is shown in Eq. 4 and is consistent with the STAR result within uncertainties.

$$B_{ee}\frac{\mathrm{d}\sigma_{J/\psi}}{\mathrm{d}y} = 42.5 \pm 1.4 \ \text{(stat.)} \pm 4.8 \ \text{(syst.)} \pm 3.1 \ \text{(glob.) nb.} \quad (4)$$

The p_T spectra provide valuable information about the J/ψ production mechanism and J/ψ interaction with the nuclear medium. The p_T distribution is broadened in A+A and d+Au with respect to p+p probably due to the Cronin effect, which arises from the multiple parton scattering in the initial state [15]. This broadening can be described by the formula: $\langle p_T^2 \rangle_{AA} = \langle p_T^2 \rangle_{pp} + N_c^{AA}\delta_0$, where N_c^{AA} is the average number of collisions for the projectile parton with target partons and δ_0 is the average increase in p_T a parton receives per collision. By comparing $\langle p_T^2 \rangle$ in different collision systems (p+p, p+A, A+A) the parameter δ_0 can be obtained. Moreover, the analysis of this $\langle p_T^2 \rangle$ broadening in A+A may allow further study of the J/ψ production mechanism. It is expected [34] that J/ψ produced primarily by regeneration mechanism, will be characterized by a softer p_T spectrum (small $\langle p_T^2 \rangle$), while the direct J/ψ from the initial hard scattering will show a rather hard p_T spectrum (large $\langle p_T^2 \rangle$). Measurements of $\langle p_T^2 \rangle$ in p+p and d+Au collisions serve as a baseline for such study allowing to extract δ_0. If the observed $\langle p_T^2 \rangle$ is smaller in A+A collisions than expected from Cronin effect only, this may indicate that J/ψ regeneration is contributing to the overall production.

The J/ψ invariant cross section from STAR has been used to study the J/ψ $\langle p_T^2 \rangle$ in p+p and d+Au collisions at $\sqrt{s_{NN}} = 200$ GeV shown in Fig. 10.

The J/ψ $\langle p_T^2 \rangle$ in p+p collisions for $p_T < 14$ GeV/c was obtained directly from the STAR data, and its value is $\langle p_T^2 \rangle = 3.45 \pm 0.85$ (stat.) ± 1.22 (syst.) (GeV/c)^2. The results are consistent with PHENIX data in $|y| < 0.35$ at the same energy [35]. In d+Au, the $\langle p_T^2 \rangle$ was calculated directly from combined STAR data points for $p_T < 3$ GeV/c and PHENIX data for $3 < p_T < 15$ GeV/c. The $\langle p_T^2 \rangle$ was found to be $\langle p_T^2 \rangle = 3.70 \pm 0.33$ (stat.) ± 0.44 (syst.) (GeV/c)^2. The data are compared to various measurements at other collision energies obtained from the NA38, NA51, NA50 [36], E789 [37] and CDF [38] experiments in Fig. 10, and an increase of J/ψ $\langle p_T^2 \rangle$ with collision energy is observed. Our measurements are consistent with the world data trend.

The PHENIX p+p data for $p_T < 2$ GeV/c [31] and STAR data for $p_T > 2$ GeV/c [11] are combined as a p+p baseline to provide better precision for R_{dA}. The p_T-integrated nuclear modification factor for J/ψ with $p_T < 3$ GeV/c and $|y| < 1$ is shown in Fig. 11. The
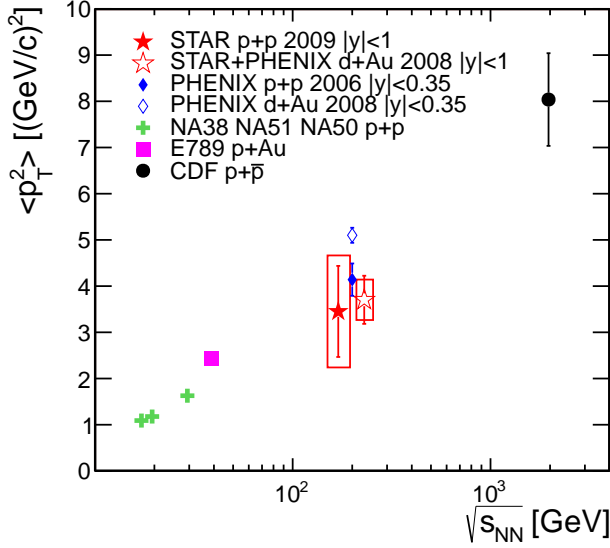
FIG. 10: (Color online) The energy dependence of J/ψ $\langle p_T^2 \rangle$. The STAR data (closed stars for $p+p$ and open stars for $d+$Au) is compared to PHENIX data [32, 35] at $\sqrt{s_{NN}} = 200$ GeV, and various measurements at other collisions energies from the NA38, NA51, NA50, E789, and CDF experiments [36–38]. The STAR results are shifted in $\sqrt{s_{NN}}$ for clarity.

FIG. 11: (Color online) The nuclear modification factor versus $N_{\rm coll}$ for J/ψ with $|y| < 1$ and $p_T < 3$ GeV/c in $d+$Au collisions (closed circles). The central green line represents the predicted shadowing based on the EPS09 nPDFs at next-to-leading order (NLO) [16, 18] while the purple line shows shadowing combined with $\sigma_{\rm abs} = 8.0$ mb, and the band indicates the uncertainty on the calculations. The data are compared to PHENIX results in $|y| < 0.35$ [39] (open circles).

normalization uncertainty from the statistical and systematic uncertainty on the J/ψ $p+p$ cross section, the uncertainty on the inelastic cross section, and the uncertainty on $N_{\rm coll}$ are indicated on the vertical axis. The STAR results are consistent with unity within the uncertainties.

The J/ψ nuclear modification factor for $d+$Au has been compared to model calculations for cold nuclear matter effects on J/ψ production in $d+$Au collisions. The CNM effects include the modification of nuclear parton distribution functions obtained from the EPS09 [16] and nDSg [17] parameterizations as well as effective J/ψ absorption cross section ($\sigma_{\rm abs}$) [6, 18] . The absorption cross section was obtained by treating it as a free parameter in a χ^2 minimization fit of the model calculations including CNM effects to the data. The χ^2 from the fit between the STAR data and model calculations as a function of the absorption cross section is shown in Fig. 12 for the EPS09 and nDSg calculations of the nPDFs. The absorption cross section of $\sigma_{\rm abs} = 0.0^{+3.8}_{-0.0}$ (stat.) $^{+2.1}_{-0.0}$ (syst.) mb was obtained from the minimum χ^2 value between the data and EPS09, which yields moderate χ^2 compared to nDSg. By taking the minimum χ^2+1 (green dashed line), a 3.8 mb statistical and 2.1 mb systematic uncertainty related to the fitting procedure was obtained. Due to the large uncertainties we quote an upper limit for nuclear absorption cross section of $\sigma_{\rm abs} = 8.7$ mb at 2σ confidence interval. The value for the absorption cross section is consistent with the results obtained using the
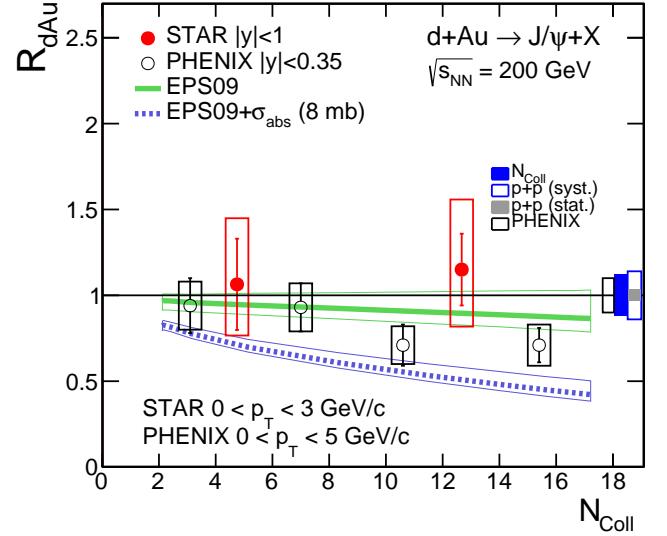
nDSg parameterization and with other calculations performed at the same energy [32, 39]. The calculated R_{dA}, assuming only shadowing and using the EPS09 nPDFs with the CTEQ6.1M free proton PDF at next-to-leading order (NLO) [16], is shown in Fig. 11 as the green solid line. The bands indicate the uncertainty from the EPS09 nPDFs. The model calculations agree with the data within the uncertainties. The EPS09 model calculations, with and without a nuclear absorption cross section of $\sigma_{\rm abs} = 8.0$ mb (within 1.84σ of our confidence interval) are also shown in Fig. 11.

The p_T dependence of the J/ψ nuclear modification factor in $|y| < 1$ for $0 - 100\%$ centrality in $\sqrt{s_{NN}} = 200$ GeV collisions is shown in Fig. 13. The grey band represents the statistical uncertainty on the J/ψ $p+p$ cross section measurement. The normalization uncertainties from the systematic uncertainty of the J/ψ $p+p$ cross section and the uncertainty of $N_{\rm coll}$ are indicated on the vertical axis. The results are compared to PHENIX data in $|y| < 0.35$ and are in agreement within statistical and systematic uncertainties. The model calculations assuming shadowing only (EPS09) and shadowing combined with an absorption cross section $\sigma_{\rm abs} = 8$ mb are also shown and both are consistent with the data. Note, that PHENIX results indicate suppression below p_T of 2 GeV/c.
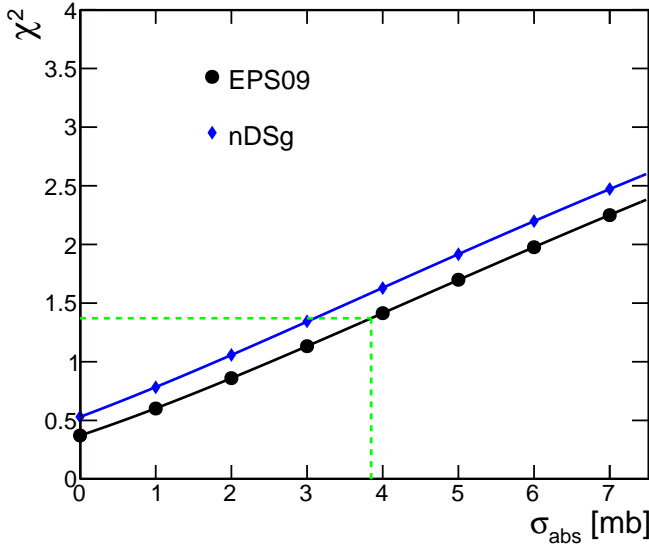
FIG. 12: (Color online) The χ^2 of the model calculations fitted to the STAR J/ψ R_{dA} using the EPS09 [16, 18] and nDSG [6, 17] nPDFs as a function of a J/ψ absorption cross section σ_{abs}. The green dashed vertical and horizontal lines show the uncertainty on the σ_{abs} and minimum χ^2+1 respectively for the EPS09.

section as a free parameter. An upper limit $\sigma_{abs} = 8.7$ mb within a 2σ confidence interval was obtained using the EPS09 calculations.
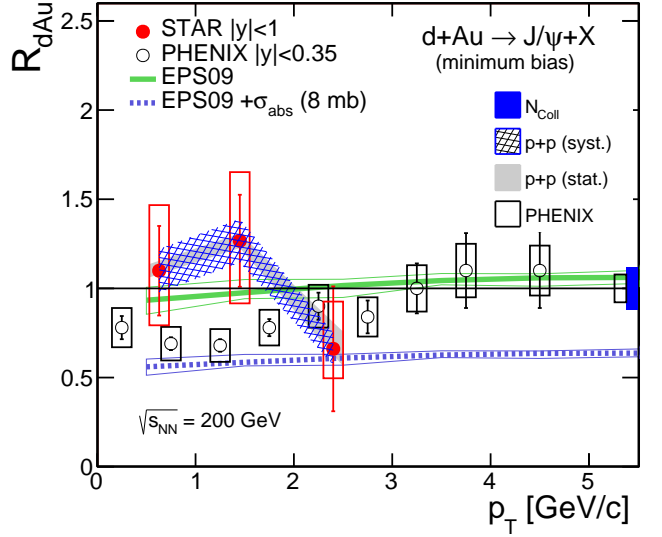

FIG. 13: (Color online) The nuclear modification factor versus transverse momentum for J/ψ with $|y| < 1$ in 0-100% central d+Au collisions (closed circles). The central green line represents the calculated shadowing based on the EPS 09 nPDFs at next-to-leading order (NLO) [16] combined with a J/ψ absorption cross section of $\sigma_{abs} = 0$ mb [18] while the purple line shows shadowing combined with $\sigma_{abs} = 8.0$ mb, and the band indicates the uncertainty on the calculations. The data are compared to PHENIX data in $|y| < 0.35$ [32] (open circles).

VI. SUMMARY

The production of J/ψ within $|y| < 1$ for $p_T < 4$ GeV/c in p+p and $p_T < 3$ GeV/c in d+Au collisions at $\sqrt{s_{NN}} = 200$ GeV, measured via the dielectron decay channel in the STAR detector, have been presented. The J/ψ p_T spectrum in p+p collisions at STAR has been extended to cover $0 < p_T < 14$ GeV/c and has been used to calculate the J/ψ $\langle p_T^2 \rangle$ in p+p collisions at $\sqrt{s_{NN}} = 200$ GeV. The results are consistent with other measurements at the same energy. The obtained $\langle p_T^2 \rangle$ in d+Au of $\langle p_T^2 \rangle = 3.70 \pm 0.33$ (stat.)± 0.44 (syst.) (GeV/c)^2 is consistent with the p+p result of $\langle p_T^2 \rangle = 3.45 \pm 0.85$ (stat.) ± 1.22 (syst.) (GeV/c)^2 within large uncertainties, suggesting no significant Cronin effect. The $\langle p_T^2 \rangle$ has also been compared to results from various experiments and exhibits an increase with increasing collision energy. The STAR data are consistent with the world data trend. The modification of J/ψ production in d+Au is consistent with no suppression within the measured uncertainties. The results have been compared to model calculations using the EPS09 and nDSg parameterizations of the nPDFs including a J/psi nuclear absorption cross

VII. ACKNOWLEDGEMENTS

[1] J. Adams et al. (STAR Collaboration), Nucl. Phys. A **757**, 102 (2005).

[2] K. Adcox et al. (PHENIX Collaboration), Nucl. Phys. A **757**, 184 (2005).

[3] I. Arsene et al. (BRAHMS Collaboration), Nucl. Phys. A **757**, 1 (2005).

[4] B. Back et al. (PHOBOS Collaboration), Nucl. Phys. A **757**, 28 (2005).

[5] T. Matsui and H. Satz, Phys Lett. B **178**, 416 (1986).

[6] R. Vogt, Phys. Rev. C **71**, 054902 (2005).

[7] J. V. Noble, Phys. Rev. Lett. **46**, 412 (1981).

[8] V. Tram and F. Arleo, Eur. Phys. J. C **61**, 847 (2009).

[9] B. Kopeliovich, I. Potashnikova, and I. Schmidt, Phys. Lett. A: **864**, 203 (2011).

[10] B. Kopeliovich, I. Potashnikova, and I. Schmidt, Phys. Rev. C: **82**, 024901 (2010).

[11] L. Adamczyk et al. (STAR Collaboration), Phys. Lett. B **722**, 55 (2013).

[12] Y.-Q. Ma and R. Venugopalan, Phys.Rev.Lett. **113**, 192301 (2014).

[13] Y.-Q. Ma et al., Phys.Rev.Lett. **106**, 042002 (2011).

[14] R. E. Nelson, R. Vogt, and A. D. Frawley, Phys. Rev. C **87**, 014908 (2013).

[15] L. Kluberg and H. Satz (2009), arXiv:0901.3831v1.

[16] K. Eskola, H. Paukkunen, and C. Salgado, Nucl. Phys. A **830**, 599 (2009).

[17] D. de Florian and R. Sassot, Phys. Rev. D **69**, 074028 (2004).

[18] R. Vogt, Phys. Rev. C **81**, 044903 (2010).

[19] K. H. Ackermann et al., Nucl. Instr. Meth. A **499**, 624 (2003).

[20] B. Bonner et al., Nucl. Instr. Meth. A **508**, 181 (2003).

[21] K. H. Ackermann et al., Nucl. Instr. Meth. A **499**, 713 (2003).

[22] W. J. Llope et al., Nucl. Instr. Meth. A **522**, 252 (2004).

[23] C. Adler et al., Nucl. Instr. Meth. A **499**, 433 (2003).

[24] L. Adamczyk et al. (STAR Collaboration), Phys. Rev. D **86**, 072013 (2012).

[25] M. Beddo et al., Nucl. Instr. Meth. A **499**, 725 (2003).

[26] B. Abelev et al. (STAR Collaboration), Phys. Rev. C **79**, 034909 (2009).

[27] M. L. Miller et al., Ann. Rev. Nucl. Part. Sci. **57**, 205 (2007).

[28] K. Olive et al. (Particle Data Group), Chin. Phys. C **38**, 090001 (2014).

[29] H. Bichsel, Nucl. Instr. Meth. A **562**, 154 (2006).

[30] J. Adams et al. (STAR Collaboration), Phys. Rev. Lett. **91**, 172302 (2003).

[31] A. Adare et al. (PHENIX Collaboration), Phys. Rev. D. **82**, 012001 (2010).

[32] A. Adare et al. (PHENIX Collaboration), Phys. Rev. C **87**, 034904 (2013).

[33] R. L. Thews, M. Schroedter, and J. Rafelski, Phys. Rev. C **63**, 054905 (2001).

[34] L. Grandchamp and R. Rapp, Nucl. Phys. A **709**, 415 (2002).

[35] A. Adare et al. (PHENIX Collaboration), Phys. Rev. Lett. **98**, 232301 (2007).

[36] O. Drapier (NA50 Collaboration) (1998), URL http://na50.web.cern.ch/NA50/theses.html.

[37] M. H. Schub et al. (E789 Collaboration), Phys. Rev. D **52**, 1307 (1995).

[38] D. Acosta et al. (CDF Collaboration), Phys. Rev. D **71**, 032001 (2005).

[39] A. Adare et al. (PHENIX Collaboration), Phys. Rev. C **77**, 024912 (2008), erratum-ibid. Phys. Rev. **C** 79, 059901 (2009).